

## Article

# Modeling and Analysis of the Drying Process of Lithium-Ion Battery Electrodes Based on Non-Steady-State Drying Kinetics

Chunhui Zhao <sup>1</sup>, Yuxin Zhang <sup>1</sup>, Xiaozhong Du <sup>1,2,\*</sup>, Jianjun Zhao <sup>1</sup> and Yijian Hu <sup>1</sup><sup>1</sup> School of Mechanical Engineering, Taiyuan University of Science and Technology, Taiyuan 030024, China<sup>2</sup> School of Energy and Materials Engineering, Taiyuan University of Science and Technology, Jincheng 048000, China

\* Correspondence: xiaozhong\_d@163.com

**Abstract:** The drying process of lithium-ion battery electrodes is one of the key processes for manufacturing electrodes with high surface homogeneity and is one of the most energy-consuming stages. The choice of the drying parameters has a significant impact on the electrode properties and the production efficiency. In response to these issues, this study establishes the non-steady-state drying kinetic equation for the electrodes, revealing the comprehensive effects of various dominant factors on the drying process. The drying rate is closely related to the electrode surface temperature, thickness, and other factors. Furthermore, this study proposes a coupled model of hot air drying field and capillary porous electrode solvent evaporation. The results showed that approximately 90% of the solvent was removed in less than half of the drying time. Then, the mechanism and control factors of electrode solvent evaporation are analyzed. During the preheating phase, the drying rate is controlled by electrode heating and temperature rise. In the constant velocity phase, it is regulated by the heat transfer from the surface airflow, while in the deceleration phase, it is affected by the mass transfer from the electrodes. Additionally, the effects of different thicknesses, temperatures, and airflow speeds on the drying process were investigated. Finally, experimental verification demonstrated the optimal parameters within the scope of the study: a temperature of 363.15 K and airflow speeds of 2.3 m/s result in a higher drying rate, as well as favorable mechanical performance.



**Citation:** Zhao, C.; Zhang, Y.; Du, X.; Zhao, J.; Hu, Y. Modeling and Analysis of the Drying Process of Lithium-Ion Battery Electrodes Based on Non-Steady-State Drying Kinetics. *Processes* **2023**, *11*, 3236. <https://doi.org/10.3390/pr11113236>

Academic Editors: Michael C. Georgiadis, Luigi Piga and Hui Li

Received: 19 September 2023  
Revised: 6 November 2023  
Accepted: 14 November 2023  
Published: 16 November 2023



**Copyright:** © 2023 by the authors. Licensee MDPI, Basel, Switzerland. This article is an open access article distributed under the terms and conditions of the Creative Commons Attribution (CC BY) license (<https://creativecommons.org/licenses/by/4.0/>).

**Keywords:** lithium-ion battery; electrode manufacturing; coating drying; heat and mass transfer

## 1. Introduction

Lithium-ion batteries are widely utilized in various fields, including modern electronic products, electric vehicles, and energy storage, due to their high performance [1–3]. These batteries consist of a positive electrode, a negative electrode, a separator, and an electrolyte. Positive and negative electrodes are fabricated by blending active materials, conductive agents, and binders. The resulting slurry is then coated onto the current collector and subjected to drying [4,5]. It is crucial to ensure that the electrodes are dried in a timely manner during this process, as the solvent may contain moisture and other impurities that may adversely affect the battery performance. Therefore, the drying of the electrodes plays a crucial role in the fabrication of intelligent electrodes [6]. To better control the performance of the electrodes, it is necessary to enhance the understanding of the drying dynamics [7].

In the study of drying techniques for lithium batteries, the key point is the relationship between the amount of electrode dewatering and various dominant factors during drying. These factors can be categorized into two main aspects: first, the intrinsic properties of the slurry, including intrinsic factors such as structural characteristics, physical and chemical properties, and thermophysical properties. This is followed by drying conditions, which encompass external factors such as drying parameters and drying methods. Drying parameters include heating temperature, heating power, dry-bulb and wet-bulb temperatures,

and airflow direction and velocity. Drying methods comprise constant condition drying, variable condition drying, as well as rapid or moderate heating, constant insulation time, and cooling methods, etc. [8]. Commonly used drying methods include infrared drying, hot air drying, thermoelectric drying [9], etc.

The drying of electrodes is a typical non-steady-state process, and studying its characteristics holds significant value for both practical and theoretical purposes [10]. As early as 1957, Zhang Hong yuan et al. [11] pointed out from a physical perspective that the drying rate is a comprehensive indicator for describing the drying process, with the surrounding medium playing a crucial role. Traditional drying theories primarily focus on drying kinetics experiments conducted under constant conditions [12,13]. Currently, there are numerous research reports on non-steady-state drying, with a significant emphasis on experimental studies [14,15]. Zhu et al. [16] found that higher drying temperatures result in excessive internal stress in the electrode and reduced electrode adhesion. Excessive temperature causes the electrode surface to harden, resulting in electrode cracking and wrinkling. However, Yang Junhong et al. [17] also emphasized the significance of variable temperature drying through their experimental investigation. Jaiser et al. [18] implemented variable temperature drying in the production of lithium battery electrodes and experimentally confirmed its benefits in terms of energy savings and improved electrode performance. Most of these literature focus on the experimental study of the correlation between the variation of the binder concentration within the electrode during drying and its connection to the electrode quality, energy consumption, and economic requirements. However, few studies have investigated the electrode drying process of lithium battery electrodes by analyzing the heat and mass transfer inside the coating, and summarized the influence law of drying parameters, which will be the focus of this study.

The main focus of this research is to establish the non-steady-state drying kinetics equation for electrodes and develop a coupled model of hot air drying field and capillary porous electrode solvent evaporation. The physical processes of mass transfer and heat transfer during drying of a battery electrode are investigated. It involves an in-depth analysis of the effect of different parameters such as the temperature of the hot air, the velocity of the hot air, and the thickness of the electrodes on the drying rate. In addition, it includes simulation, prediction, and optimization of the drying process to provide better guidance and optimization solutions.

## 2. Non-Steady-State Drying Kinetics Equation

Electrodes belong to the class of capillary porous medium colloids and the drying process is complex, involving simultaneous heat and mass transfer of solids, liquids, and gases. Therefore, equations established based solely on constant parameters are independent of heating conditions, limiting the accuracy and applicability of their analysis results [19]. Investigating the relationship between the amount of instantaneous dehydration of a material during drying and various governing factors falls within the scope of drying dynamics. Hence, this study establishes a non-steady-state drying kinetics equation for the drying dynamics between the instantaneous amount of dehydration and various governing factors.

See Figure 1 for a schematic view of the electrode with the equations established. After the electrode enters the drying chamber, it continues to move steadily and homogeneously under the action of the circulating heated air, receiving energy and undergoing dehydration. The energy received by the electrode includes convective heat transfer from the air on the electrode surface  $Q_1$ , the energy that heats electrode  $Q_2$ , the energy consumed to overcome the binding energy during solvent separation  $Q_3$ , and the heat absorption from moisture evaporation  $Q_4$ .  $\Delta Q$  represents energy loss, assuming  $\Delta Q = 0$ , which means:

$$Q_1 = Q_2 + Q_3 + Q_4 \quad (1)$$

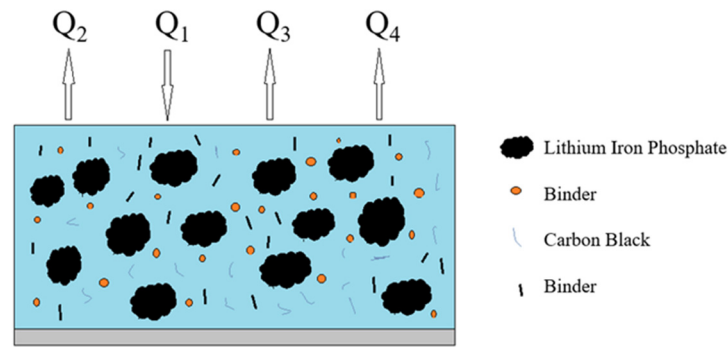


**Figure 1.** Schematic of the electrode energy.

1. Thermal convective heat transfer  $Q_1$ :

$$Q_1 = \int_F \alpha_1 (t_{di} - t_{si}) \cdot dF \quad (2)$$

where  $t_{di}$  is the instantaneous dry bulb temperature of air,  $t_{si}$  is the instantaneous surface temperature of the electrode,  $\alpha_1$  is the pair heat transfer coefficient,  $F$  is the surface area of the electrode.

2. Heat absorption during electrode heating  $Q_2$ :

$$Q_2 = (C_a + xC_w)G_0 \left( \frac{d_t}{d_\tau} \right) \quad (3)$$

where  $C_a$  is the specific heat of absolute dry slurry,  $x$  is the moisture content of the dry basis,  $C_w$  is the specific heat of solvent,  $G_0$  is the absolute dry mass of the slurry,  $t$  is the average surface temperature of the electrode,  $\tau$  is time.

3. The energy of the solvent to overcome the binding energy when it is removed from the slurry  $Q_3$ :

$$Q_3 = \Delta\gamma \frac{dM}{d\tau} \quad (4)$$

where  $\Delta\gamma$  is the binding energy of solvent and slurry,  $dM$  is the amount of solvent removed.

4. Heat of solvent vaporization absorption  $Q_4$

$$Q_4 = \gamma_w \frac{dM}{d\tau} \quad (5)$$

where  $\gamma_w$  is the latent heat of vaporization of the solvent at the surface temperature of the electrode.

Because,

$$G_w = G_0(1 + x) \quad (6)$$

where  $G_w$  is the mass of wet slurry,  $G_w = F\delta\rho_w$

Therefore,  $G_0 = \frac{G_w}{(1+x)}$ .

Substituting Equations (2)–(6) into Equation (1), the following is obtained:

$$\frac{dM}{G_0 d\tau} = \frac{1+x}{\delta\rho_w(\gamma_w + \Delta\gamma)} (\alpha_1(t_{di} - t_{si})) - (C_a + xC_w) \left( \frac{d_t}{d_\tau} \right) / (\gamma_w + \Delta\gamma) \quad (7)$$

where  $\frac{dM}{G_0 d\tau}$  is the drying rate, which was measured with dry slurry as a reference basis. Denote the rate at which the moisture mass per unit mass of dry slurry undergoing vaporization changes during a given time period.

Equation (7) represents the non-steady-state drying kinetics equation, which reflects the various governing factors influencing the drying process. The drying rate depends on the surface temperature of the electrodes and is a function of the drying-bulb temperature. Moreover, it is proportional to the initial moisture content of the slurry and inversely proportional to the thickness of the electrode.

### 3. Electrode Drying Model

#### 3.1. Method

The volume-averaging method is employed in this study to characterize the solvent evaporation model within capillary porous electrodes [20–23]. The primary is to establish a fundamental understanding of solvent drying phenomena within the electrodes. To facilitate a more intuitive representation, a two-dimensional model of the drying process is constructed for a selected portion of the interior of the drying chamber, and the coating with solvent is represented by an unsaturated porous medium. To maintain the simplicity of the model and computational feasibility, the following additional assumptions are made [20,23,24]:

- (1) Since the adhesive mass fraction is generally  $\leq 2\%$ , it is considered that the solvent does not contain any adhesive/polymer.
- (2) The active particles are homogeneous and spherical, and the permeability and other parameters are isotropic throughout the porous medium.
- (3) The liquid and air/vapor phases are continuous.
- (4) Darcy's law applies to the gas and liquid phases.
- (5) The binary air/vapor mixtures behave like ideal gases, and Fick's law is applicable for describing diffusion between air and vapor.
- (6) Energy transfer occurs through conduction in the three phases and through liquid and gas convection. Thermal properties, such as specific heat and thermal conductivity, remain constant over the drying temperature range.

Figure 2 shows the electrode models with different thicknesses.

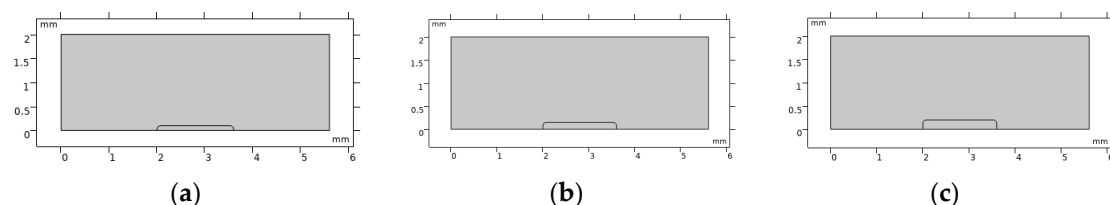


**Figure 2.** Electrodes with different thicknesses: (a) 100  $\mu\text{m}$ -thick electrode, (b) 150  $\mu\text{m}$ -thick electrode, (c) 200  $\mu\text{m}$ -thick electrode.

#### 3.2. Mathematical Formulation

The governing equations are derived in the framework of continuity for an electrode drying system consisting of solid, liquid, and gas phases. The total volume of the computational cell  $\Delta V$  is defined as:

$$\Delta V = \Delta V_s + \Delta V_l + \Delta V_g \quad (8)$$

where  $\Delta V_s$ ,  $\Delta V_l$ , and  $\Delta V_g$  represent the unit volumes of the solid phase, liquid phase, and gas phase, respectively. Assuming  $\varepsilon_s$  is the volume fraction of solid in the system, the porosity  $\varepsilon$  is introduced to represent the voids filled with liquid and gas. Saturation (S) is defined as the volume fraction of liquid in the voids [25,26]. Therefore, the porosity  $\varepsilon$  and the saturation S are expressed as:

$$\varepsilon = 1 - \varepsilon_s \quad (9)$$

$$S = \frac{\text{volume of liquid}}{\text{volume of void space}} \quad (10)$$

Currently, the solvent mass conservation equations are written for both liquid and vapor phases. Under electrode drying, the mass conservation equation for the liquid phase is defined as follows,

$$\frac{\partial}{\partial t}(\rho_l \varepsilon S_l) + \frac{\partial}{\partial x}(c_l) = -\dot{m} \quad (11)$$

where  $\rho_l$  is the density of the liquid phase,  $c_l$  is the total flux of the liquid phase, and  $\dot{m}$  is the evaporation rate. In the given Equation (12),  $c_l$  can be decomposed into the convective flux of the liquid phase  $c_l^{\text{press}}$  and the capillary flux of the liquid phase  $c_l^{\text{cap}}$ , which are calculated using Darcy's law, where  $P_g$  is the gas phase pressure,  $\mu_l$  is the liquid phase viscosity, and  $x$  is the coordinate in the thickness direction. As shown in Equations (13)–(16), the capillary flux of the liquid phase is represented by the capillary diffusion coefficient  $D_l$ , which is the partial derivative of the liquid phase saturation  $S_l$ . The capillary pressure  $P_c$  is calculated using the Leverett model according to Equation (15) [20,27,28], where  $\sigma$  represents the liquid surface tension,  $S_{le}$  represents the final saturation of the liquid phase, and  $K_l$  and  $K_{al}$  represent the liquid phase permeability and absolute permeability.

$$c_l = c_l^{\text{press}} + c_l^{\text{cap}} = -\rho_l \frac{k_l}{\mu_l} \frac{\partial P_g}{\partial x} + \rho_l \frac{k_l}{\mu_l} \frac{\partial P_c}{\partial x} \quad (12)$$

$$c_l^{\text{cap}} = -\rho_l D_l \varepsilon \frac{\partial S_l}{\partial x} \quad (13)$$

$$D_l = -\frac{k_l}{\varepsilon \mu_l} \frac{\partial P_c}{\partial S_l} \quad (14)$$

$$P_c = \sqrt{\frac{\varepsilon}{K_{al}}} f(S_l) \sigma \quad (15)$$

$$f(S_l) = 0.221(1 - S_l) + 0.364(0 - e^{-40(1-S_l)}) + \frac{1}{200(S_l - S_{le})} \quad (16)$$

The mass conservation equations for solvent vapor and gaseous air during electrode drying are as follows:

$$\frac{\partial}{\partial t}(\rho_v \varepsilon (1 - S)) + \frac{\partial}{\partial x}(c_v) = \dot{m} \quad (17)$$

$$\frac{\partial}{\partial t}(\rho_a \varepsilon (1 - S)) + \frac{\partial}{\partial x}(c_a) = 0 \quad (18)$$

where  $\rho_v$  is the density of vapor,  $\rho_a$  is the density of air. The pressure convection and diffusion parts of the total mass flux of solvent vapor  $c_v$  and the total mass flux of gas phase air  $c_a$  can be obtained by Darcy's law and the molecular diffusion law (Fick's law), respectively [23,29]:

$$c_v = c_v^{\text{press}} + c_v^{\text{cap}} = -\rho_v \frac{k_g}{u_g} \frac{\partial P_g}{\partial x} - \frac{\varepsilon(1 - S_l)\rho_g}{M_g^2} M_a M_v D_{av} \frac{\partial}{\partial x} \left( \frac{\rho_v}{\rho_g} \right) \quad (19)$$

$$c_a = c_a^{\text{press}} + c_a^{\text{cap}} = -\rho_a \frac{k_g}{u_g} \frac{\partial P_g}{\partial x} - \frac{\varepsilon(1 - S_l)\rho_g}{M_g^2} M_a M_v D_{av} \frac{\partial}{\partial x} \left( \frac{\rho_a}{\rho_g} \right) \quad (20)$$

where  $c_v^{\text{press}}$  and  $c_v^{\text{cap}}$  represent the mass flux of solvent vapor caused by gas pressure and molecular diffusion, while  $c_a^{\text{press}}$  and  $c_a^{\text{cap}}$  represent the mass flux of gaseous air caused by gas pressure and molecular diffusion,  $k_g$  and  $u_g$  are the viscosity and permeability of the gas phase, respectively.  $M_a$ ,  $M_v$ ,  $M_g$ , and  $D_{av}$  are the molecular weights of air, vapor, gas phases, and the air–vapor diffusion coefficient.

The energy conservation equation is as follows:

$$(\rho C_p) \frac{\partial T}{\partial t} + h_{\text{vap}} \dot{m} = \frac{\partial}{\partial x} \left( \lambda \frac{\partial T}{\partial x} \right) \quad (21)$$

where  $h_{\text{vap}}$  is the evaporative heat of the solvent. Additionally, Equations (21) and (22) represent the effective specific heat capacity,  $\rho C_p$ , and effective thermal conductivity,  $\lambda$ , of the electrode as a whole, respectively.

$$\rho C_p = \rho_l C_{pl} \varepsilon S_l + \rho_s C_{ps} (1 - \varepsilon) + (\rho_v C_{pv} + \rho_a C_p) \varepsilon S_g \quad (22)$$

$$\lambda = \lambda_s (1 - \varepsilon) + \lambda_l S_l \varepsilon + \lambda_g S_g \varepsilon \quad (23)$$

where  $C_{pl}$ ,  $C_{ps}$ ,  $C_{pv}$  are the specific heat capacities of the liquid phase, vapor phase, air, and solid phase, respectively, while  $\lambda_s$ ,  $\lambda_g$ ,  $\lambda_l$  are the thermal conductivities of the solid, liquid, and gas phases, respectively.

During drying of the electrode, it undergoes significant shrinkage. To explain the volume shift of the electrode during drying, we assume the variation equations for porosity ( $\varepsilon$ ) and thickness ( $h$ ) as follows:

$$\varepsilon = \varepsilon_0 - \frac{(\varepsilon_0 - \varepsilon_e)}{(S_{l0} - S_{le})} (S_{l0} - S_l) \quad (24)$$

$$h = h_0 - \frac{(h_0 - h_e)}{(\varepsilon_0 - \varepsilon_e)} (\varepsilon_0 - \varepsilon) \quad (25)$$

where  $\varepsilon_0$ ,  $\varepsilon_e$  are the initial and final porosities, respectively,  $S_{l0}$ ,  $S_{le}$  are the initial and final liquid phase saturations, and  $h_0$ ,  $h_e$  are the initial and final thicknesses of the electrode.

### 3.3. Boundary and Initial Conditions

The electrode's bottom (substrate surface,  $x = 0$ ) acts as the boundary condition, resulting in no occurrence of mass and energy exchange [23,30]. The boundary conditions are specified as follows.

$$\begin{cases} c_i = 0 & i = v, a, l \\ \lambda \frac{\partial T}{\partial t} = 0 \end{cases} \quad (26)$$

The boundary conditions at the electrode surface ( $x = l$ ) are given by Equation (20) [23,30]. The liquid phase solvent is transported upwards inside the electrode and completely evaporates at the surface, while the electrode surface is exposed to a convective flow. The surface gas pressure is equal to the atmospheric pressure.

$$\begin{cases} c_v + c_l = \varepsilon (\rho_v - \rho_{\text{vatm}}) H_m \\ \lambda \frac{\partial T}{\partial t} = H_t (T_{\text{atm}} - T) - h_{\text{vap}} c_l \\ P_g = P_{\text{atm}} \end{cases} \quad (27)$$

where  $H_m$ ,  $H_t$  are the mass transfer coefficient and heat transfer coefficient,  $\rho_{\text{vatm}}$  is the steam density in the dry airflow, and  $P_{\text{atm}}$  is the atmospheric pressure.

Finally, the initial conditions of the model are defined, containing three independent variables: temperature, pressure, and humidity distribution.

$$\begin{cases} S_l = S_{l0} \\ P_g(x, 0) = P_{\text{atm}} \\ T(x, 0) = T_{\text{initial}} \end{cases} \quad (28)$$

where  $T_{\text{initial}}$  is the initial electrode temperature.

#### 4. Analysis of Simulation Results

The coupled partial differential equations of the above model are solved using finite element methods. The parameters in the capillary porous electrode solvent evaporation model listed in Table 1 were employed during the simulation process [20,22,31]. The active material used in the model is lithium iron phosphate, and the positive electrode slurry is assumed to consist of about 60% solid particles. The solvent was N-methyl pyrrolidone (NMP).

**Table 1.** Constant numerical physical property parameters.

Parameters	Values	Parameters	Values
Liquid phase	NMP		
Molecular weight	0.099 kg/mol	Viscosity	$4.85 \times 10^{-4}$ kg/(m·s)
Absolute permeability	$5 \times 10^{-14}$ m <sup>2</sup>	Specific heat capacity	$8 \times 10^3$ J/(kg·K)
Thermal conductivity	0.1329 W/(m·K)	Density	824 kg/m <sup>3</sup>
Enthalpy of vaporization	$0.542 \times 10^6$ J/kg	diffusivity	$1 \times 10^{-5}$ m <sup>2</sup> /s

The operational airflow speed range for the actual production of lithium battery electrodes is 1.2–2.0 m/s. In this experiment, we have chosen three distinct levels of thermal airflow speed: 1.1 m/s, 1.7 m/s, and 2.3 m/s. In the practical production process of lithium battery electrodes, it is customary to subject the electrodes to drying treatment at temperatures ranging from 343.15 K to 363.15 K. For the purpose of this study, we have selected three distinct temperature conditions: 353.15 K, 363.15 K, and 373.15 K.

##### 4.1. Electrode Drying Process

The model assumes that the liquid and gas phase solvents are initially uniformly and continuously distributed within the electrode, allowing for simultaneous evaporation at all locations within the electrode. The initial solvent saturation is illustrated in Figure 3.

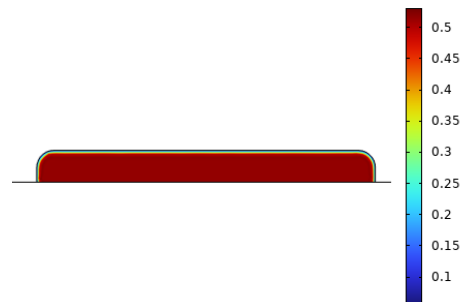


**Figure 3.** The initial solvent saturation.

Figure 4 shows that the solvent evaporation curve of the electrode is divided into three well-defined phases.

During the preheating stage from time( $t$ ) = 0 to 5 s, the electrode temperature is the main controlling factor. As the hot air transfers heat to the electrodes, its temperature increases, leading to slight shrinkage in the electrode thickness. In this stage, the liquid solvent exhibits elevated saturation, along with a relatively large capillary diffusion coefficient and low capillary pressure. At this moment, the liquid phase easily migrates to the surface and evaporates. As a result, the drying rate is mainly limited by the surface evaporation rate, which is directly related to the electrode temperature. Moreover, as the electrode temperature gradually increases from 293.15 K to approximately 341 K, the liquid phase evaporation rate continuously increases, leading to a continuous increase in the drying rate.

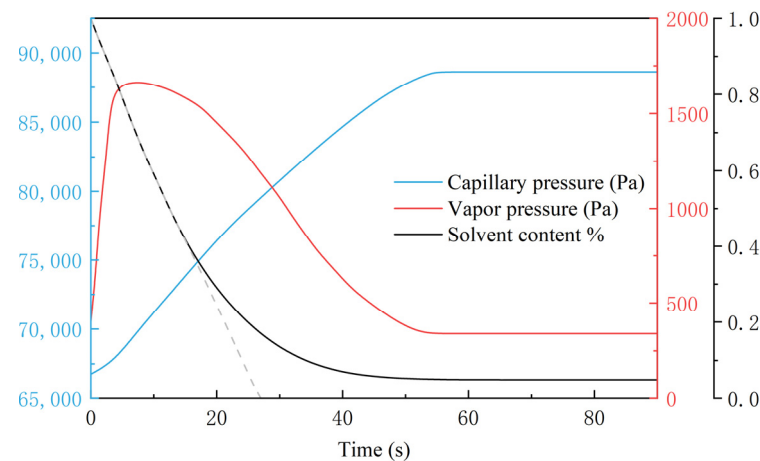


**Figure 4.** Simulated values of capillary pressure, vapor pressure, and solvent content during electrode drying process.

During the constant drying stage from 5 to 15 s, heat transfer through the air flow becomes the main controlling factor. The electrode temperature remains relatively constant, and the rate of solvent reduction (i.e., drying rate) stabilizes and reaches its maximum value. Simultaneously, the electrodes uniformly contract at a relatively fast pace, and most of the solvent evaporates during this phase. Since the heat is mainly used in the evaporation process at this time, the electrode temperature remains unchanged when it reaches a certain value. The electrode is unable to further increase the temperature-dependent vapor pressure and solvent evaporation, resulting in the drying rate remaining essentially constant. At the same time, as evaporation progresses, the solvent content and the saturation of the liquid phase gradually decrease. The capillary diffusion coefficient decreases, while the capillary pressure increases. Consequently, the liquid phase capillary diffusion flux decreases. However, there is still an adequate amount of liquid phase transport to meet the evaporation requirements.

During the deceleration drying stage from 15 to 55 s, intra-electrode mass transfer becomes the main controlling factor. The drying rate is gradually decreased until the electrodes are completely dry. At this point, the contraction rate of the electrodes slows down, representing the phase with the highest proportion of time spent in the entire drying process. During this stage, as drying progresses, some of the solvent vaporizes and exists in the form of vapor, the solvent saturation and content continuously decrease, the capillary pressure continuously increases, and the capillary diffusion coefficient and capillary diffusion flux in the liquid phase continuously decrease. At this time, since the vaporization rate at the internal liquid phase wet bulb temperature is larger than the liquid phase diffusion rate, the drying rate gradually decreases. Simultaneously, less heat is used to evaporate the solvent and the electrode temperature continues to rise, reaching a final drying temperature of 373.15 K from 341 K.

#### 4.2. Effect of Electrode Thickness on Drying Process

The temperature distribution at five different depths within the electrode is shown in Figure 5a, depicting the variation of temperature over time at the electrode–current collector interface ( $x = 0$ ), at the middle ( $x = L/4$ ), ( $x = L/2$ ), ( $x = 3L/4$ ), and at the electrode–air exposed surface ( $x = L$ ). From the graph, it can be observed that the temperature of the electrode increases rapidly in the direction of its thickness and reaches the final temperature within a short period of time. Due to the high thermal conductivity of metal oxides and solvents, the temperatures of the electrodes at different depths are nearly always consistent.

According to the trend shown in Figure 5b, within the range of electrode thicknesses investigated, the surface temperature variations of electrodes with different thicknesses exhibit a similar trend. The electrodes with thicknesses of 100  $\mu\text{m}$ , 150  $\mu\text{m}$ , and 200  $\mu\text{m}$

respectively increase rapidly from room temperature (293.15 K) to 343 K, 341 K, and 337 K. As drying progresses, their surface temperatures continue to rise until reaching 373.15 K, and then remain constant until the end of the drying process. At the same drying time, the surface temperature of the thin electrodes is higher than that of the thick electrodes. This is because thin electrodes contain less solvent and require less solvent to evaporate. Thus, under the same drying conditions, the hot air provides a constant amount of heat to heat the electrode, resulting in a higher surface temperature for the thin electrode.

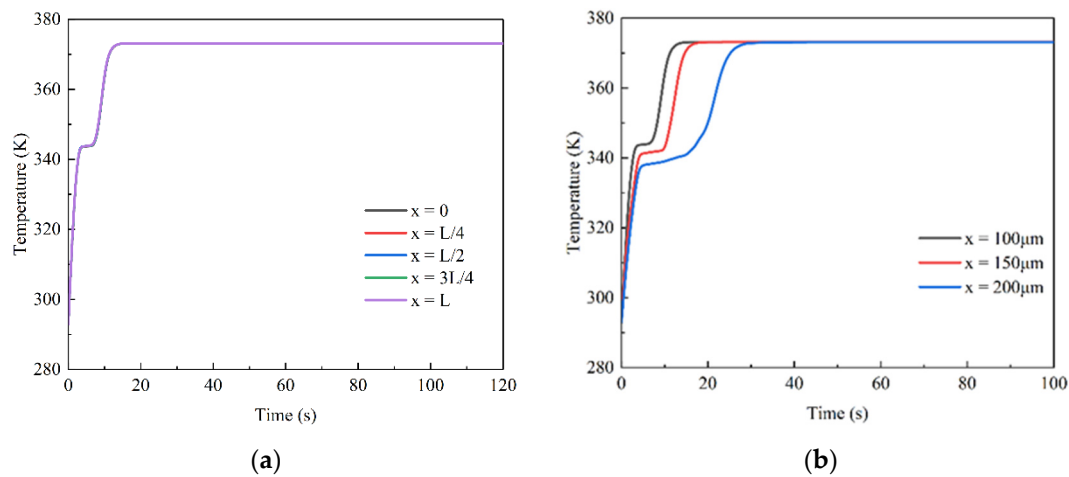


**Figure 5.** (a) Simulated temperature distribution values at different depths of the electrodes. (b) Simulated values of temperature variation on the surface of electrodes with different thicknesses.

Therefore, the electrode thickness should be reduced as much as possible to require less energy, provided that the demand is met.

#### 4.3. Effect of the Temperature of the Hot Air on the Drying Process

From Figure 6, it can be observed that, when the airflow speed is 2.3 m/s and the electrode thickness is 150  $\mu\text{m}$ , the drying time required for the electrode is 60 s, 50 s, and 45 s at drying temperatures of 353.15 K, 363.15 K, and 373.15 K, respectively. Specifically, the drying time of the electrode under the drying condition of 363.15 K is reduced by 10 s compared to the condition of 353.15 K, and it differs by only 5 s compared to the condition of 373.15 K. However, as the temperature continues to increase, the degree of reduction in drying time becomes less significant. Therefore, 363.15 K is the optimal drying temperature in the temperature range of interest.

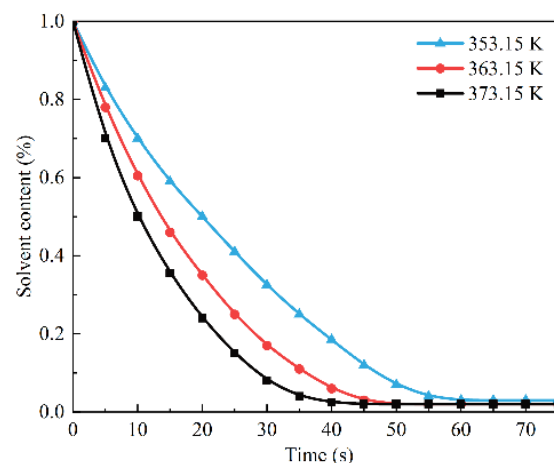


**Figure 6.** Simulation values of solvent content at three different temperatures.

#### 4.4. Effect of Hot Air Velocity on Drying Process

Figure 7a shows that, when the temperature is 363.15 K, the electrode thickness is 150  $\mu\text{m}$ , and the hot air speed is 1.1 m/s, 1.7 m/s, and 2.3 m/s, the required drying time of the electrode is 75 s, 60 s, and 50 s, respectively. This indicates that air velocity has a significant effect on the drying process. Compared to the reference air velocity of 1.7 m/s, the drying time increases by 15 s at 1.1 m/s air velocity and decreases by 10 s at 2.3 m/s air velocity. Therefore, increasing the air velocity to 2.3 m/s effectively shortens the drying time in the range of velocities studied. The reason for the shortest drying time at 2.3 m/s of hot air is the higher flow rate of hot air, which enhances mass and heat transfer at the electrode surface. As a result, there is extra thorough contact between the electrode and hot air, rapidly removing solvent from the electrode surface. This results in an increased concentration difference of solvent inside the electrode, causing rapid outward diffusion of solvent and accelerating the evaporation rate of the slurry, thus shortening the drying time.

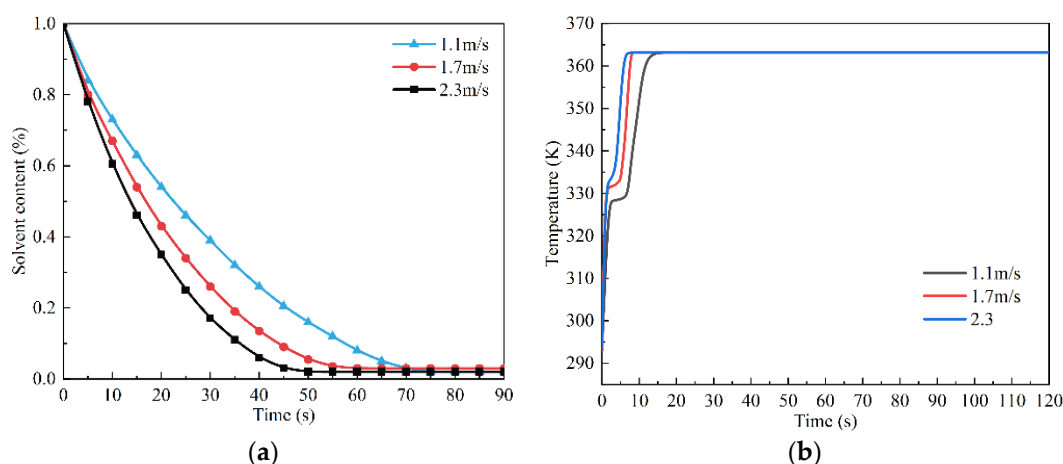


**Figure 7.** (a) Simulation values of solvent content under three different air velocities. (b) Simulated temperature values on the electrode surface at three different air velocities.

The curve shown in Figure 7b indicates that, at an air temperature of 363.15 K, the surface temperature of all electrodes initially increases rapidly, then stabilizes, and finally continues to rise and remains constant. At the same drying time, the higher the velocity of the hot air, the higher the surface temperature. This is because, as the velocity of the air increases, the amount of air reaching the electrode surface per unit time increases, resulting in a greater amount of heat being transferred to the electrode, leading to an increase in the electrode surface temperature.

## 5. Experimental Setup

To verify the accuracy of the model, electrode drying experiments were performed in this study. In addition, it was confirmed by an electron microscopy experiment that the drying of the electrodes was uniform at a temperature of 363.15 K and an air velocity of 2.3 m/s. In addition, the adhesion test experiment has confirmed that drying electrodes under the same conditions can achieve higher production efficiency.

### 5.1. Slurry Preparation

In this study, when validating the numerical model, a typical combination of lithium-ion battery cathode materials was utilized, selecting lithium iron phosphate as the active material for the cathode, carbon black as the conductive agent, polyvinylidene fluoride (PVDF) as the binder, N-methyl-2-pyrrolidone (NMP) as the solvent, aluminum foil was used as the cathode current collector. The experiment employed a double-planetary screw mixer, as illustrated in Figure 8, for stirring and mixing of the electrode slurry.



**Figure 8.** Double-planetary screw mixer.

This study utilizes a multi-step mixing process to prepare the electrode slurry. First, prepare the PVDF solution by mixing and dispersing a portion of the NMP solution and PVDF binder in a double-planetary screw mixer, with the mixing process lasting for 240 min. Next, add conductive carbon black to this solution and disperse the solution in an appropriate amount of NMP in a planetary centrifugal mixer, with the mixing process lasting for 60 min. Finally, add lithium iron phosphate in two portions and introduce an appropriate amount of NMP solution, with the mixing lasting for 120 min, to obtain the lithium iron phosphate-coated slurry for the subsequent experiments.

### 5.2. Electrode Drying Experiment

According to the given experimental procedure, using the drying chamber on the intermittent experimental coater as shown in Figure 9 to dry the electrode sheets, concurrently record the temperature of the electrode surface at different times. The experiment employed three electrodes with a thickness of 150  $\mu\text{m}$ , setting the temperature of the hot air drying chamber to 373.15 K and the wind speed to 1.7 m/s. After the start of drying, the temperature was read every ten seconds until the final set temperature was reached.

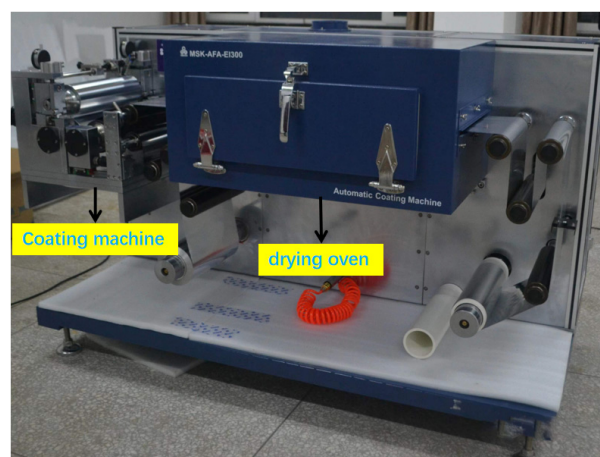


**Figure 9.** Intermittent experimental coater.

Figure 10 verifies the accuracy of the model by comparing it with experimental data. It is observed that the trends of the two sets of data are essentially consistent under the same drying parameters, especially at the onset of drying. However, there is a certain bias in the subsequent stages, which can be attributed to the fact that the model assumes ideal conditions, while the experiment fails to achieve full heat exchange. In addition, the lengthy measurement duration leads to an accumulation of measurement errors, compounded by the limited number of sampling points. Overall, the deviations of the model fall within acceptable ranges with high accuracy, making it suitable for further analysis.

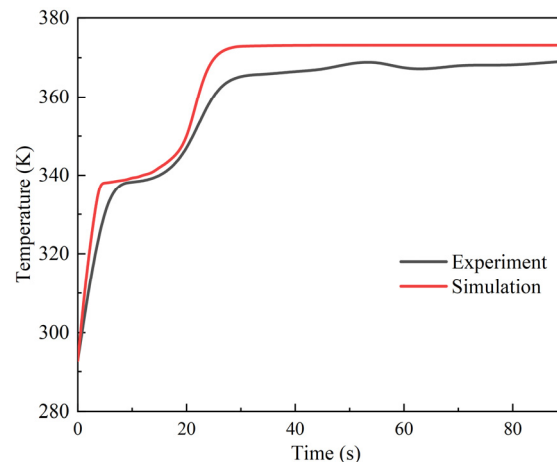


**Figure 10.** Model validation.

### 5.3. Effect of the Temperature of the Hot Air on the Drying Process

Scanning electron microscopy (SEM) images were taken of the lithium iron phosphate cathode sample. From Figure 11, it can be observed that the Li-Fe-phosphate cathode mainly consists of a bottom aluminum foil layer and an upper electrode structure. The aluminum foil layer on the bottom side has a thickness of 17  $\mu\text{m}$ , while the upper electrode has a thickness of 150  $\mu\text{m}$ . Compared to the electrode, the aluminum foil has a relatively minor impact on heat and mass transfer within the entire electrode. Thus, it is simplified by neglecting it in the previous calculations and simulations.

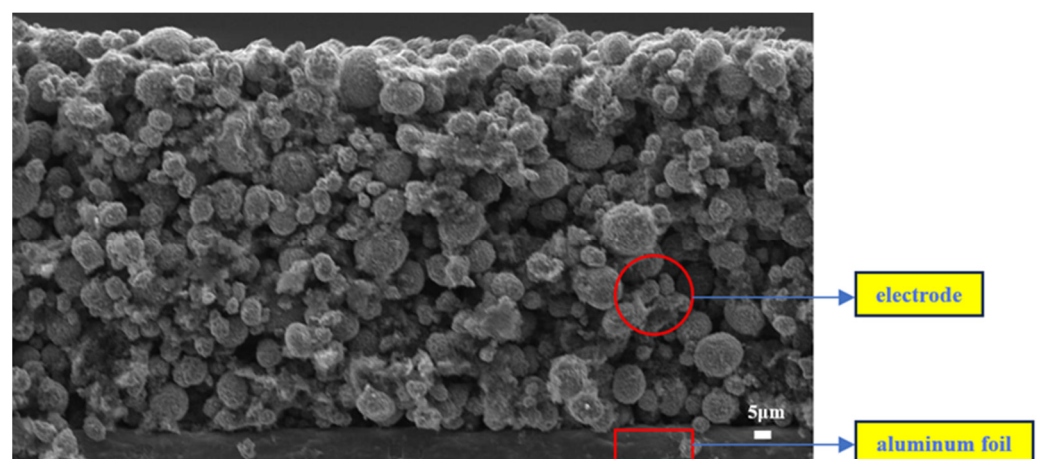


**Figure 11.** SEM at 1000 times magnification after electrode drying.

Figure 12a,b shows SEM images of the electrodes after drying. From this figure, it can be observed that: the larger particles correspond to lithium iron phosphate, while the smaller particles represent conductive agents and binders. It is important to note that the lithium iron phosphate particles exhibit uniform dispersion, and no signs of agglomeration. Therefore, it can be considered that the electrode dries uniformly at a temperature of 363.15 K and an airflow speed of 2.3 m/s within the experimental range.

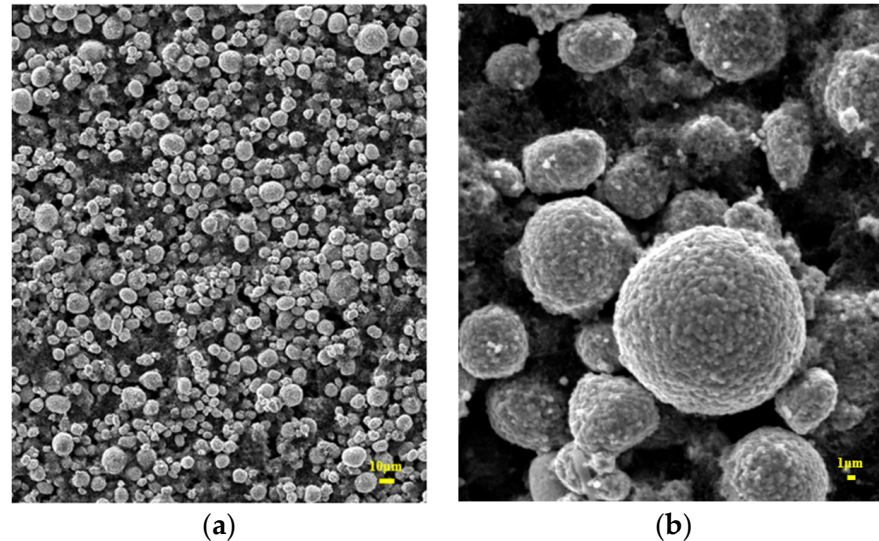


**Figure 12.** (a) SEM at 1000 times magnification after electrode drying. (b) SEM at 5000 times magnification after electrode drying.

#### 5.4. Adhesion Test Experiment

To further validate the optimal drying conditions, the adhesion of the electrodes was compared under different drying conditions (with an electrode thickness of 150  $\mu\text{m}$ ). To test the adhesion of the electrode coating using the Cross-Cut Tester, firstly, the dried electrode is securely fixed on the experimental platform. Applying uniform pressure, the electrode surface is cut with the Cross-Cut Tester. Subsequently, the electrode is rotated by  $90^\circ$ , and this operation is repeated to form a specified grid pattern on the coating surface. Then, specialized test tape is applied to the surface after cutting, ensuring complete adhesion of the tape to the electrode surface. Holding one end of the tape, it is peeled off at a 45-degree angle in an instant, and the condition of the electrode surface after peeling is observed.

Figure 13 illustrates the surface conditions of the electrodes after being subjected to the Cross-Cut Tester under different drying conditions. The results reveal that higher surface retention is observed at a temperature of 353.15 K and air velocity of 1.1 m/s and a temperature of 363.15 K and air velocity of 2.3 m/s.

In summary, within the experimental range, under drying conditions with a temperature of 363.15 K and an airflow velocity of 2.3 m/s, the electrodes are able to provide the strongest adhesion with the fastest drying rate, thus maximizing the production efficiency.

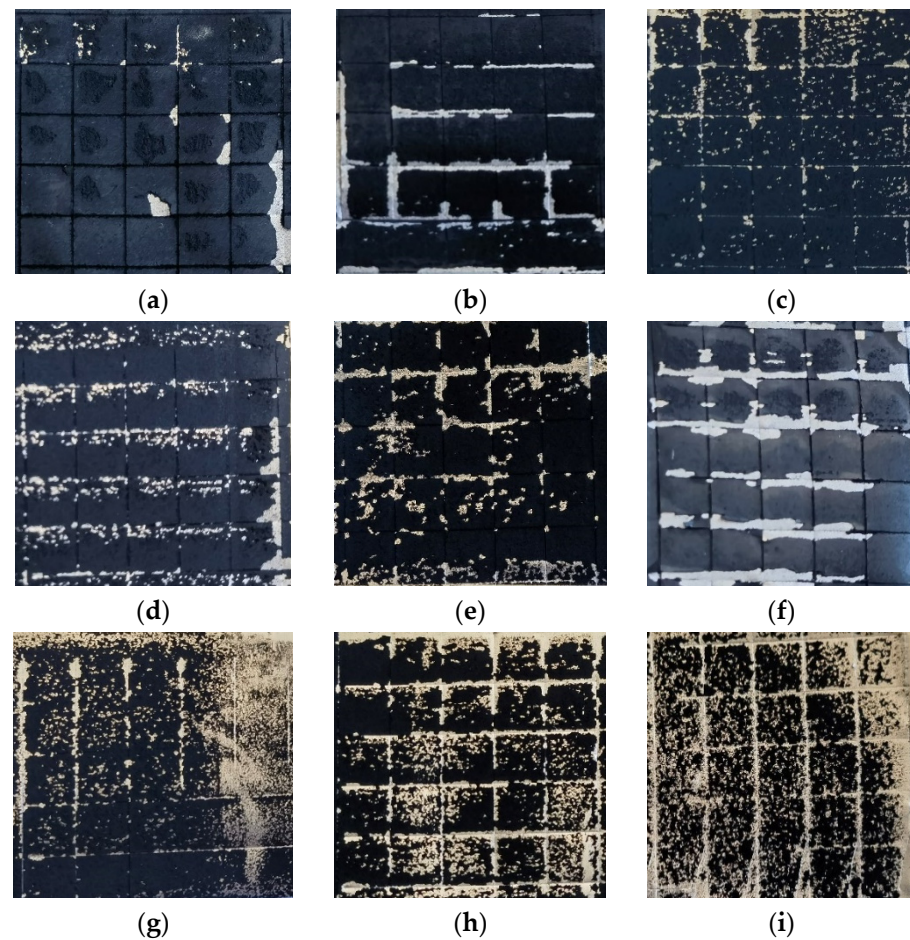


**Figure 13.** Test plots of the electrode Cross-Cut Tester under different drying conditions.: (a) 353.15 K-1.1 m/s, (b) 353.15 K-1.7 m/s, (c) 353.15 K-2.3 m/s, (d) 363.15 K-1.1 m/s, (e) 363.15 K-1.7 m/s, (f) 363.15 K-2.3 m/s, (g) 373.15 K-1.1 m/s, (h) 373.15 K-1.7 m/s, (i) 373.15 K-2.3 m/s.

## 6. Conclusions

In this study, the mechanism and limiting factors of electrode solvent evaporation are analyzed in detail using the non-steady-state drying kinetics equation and a coupled model of hot air drying field and capillary porous electrode solvent evaporation. In addition, the effect of the drying parameter on the drying process is investigated. The specific conclusions are as follows:

- (1) The electrode solvent evaporation process can be divided into three stages. Firstly, there is the preheating and temperature rise stage, during which the electrode temperature increases, and the drying speed also increases. Secondly, there is the constant-speed drying stage, where the electrode temperature remains constant, and the drying speed is at its highest. Lastly, there is the deceleration drying stage, where the electrode heats up again to the final temperature, but the drying speed gradually decreases to zero, ultimately concluding the drying process. Among these three stages, the deceleration drying stage has the longest duration.
- (2) Further analysis was conducted on the mechanism and controlling factors of electrode solvent evaporation. During the preheating phase, the drying rate is dominated by the electrode temperature. During the constant velocity phase, the drying rate is controlled by heat transfer from the surface airflow. During the deceleration phase, the drying rate is controlled by mass transfer within the electrodes.
- (3) The initial drying rate or solvent flux of the electrode coating is extremely high, and then gradually decreases. This initially high drying rate or solvent flux may potentially lead to stress-related defects or cracks within the electrode coating. To address this

issue, this study investigates the influence of various process parameters, such as hot air temperature and hot air velocity, on the solvent drying rate. Increasing the temperature facilitates faster drying, while increasing the hot air velocity enhances mass transfer coefficients, thereby accelerating the drying rate.

- (4) Finally, electron microscopy experiments and electrode adhesion experiments have verified that the drying of the electrodes at a temperature of 363.15 K and an airflow speed of 2.3 m/s resulted in a relatively high drying rate and excellent electrode quality.

This study thoroughly investigates the drying mechanism and optimal process parameters in the range studied of lithium battery electrodes, providing guidance and reference for practical production of lithium battery electrodes.

**Author Contributions:** Conceptualization, X.D. and C.Z.; methodology, C.Z.; software, C.Z.; validation, X.D. and C.Z.; formal analysis, C.Z. and Y.Z.; investigation, Y.Z. and J.Z.; resources, Y.Z.; data curation, Y.Z. and J.Z.; writing—original draft preparation, C.Z.; writing—review and editing, X.D.; visualization, Y.Z.; supervision, Y.H.; project administration, X.D.; funding acquisition, X.D. All authors have read and agreed to the published version of the manuscript.

**Funding:** This research was funded by the Natural Science Foundation of Shanxi Province, China, grant number 202103021224273; the Research Project Supported by Shanxi Scholarship Council of China, grant number 2021-137; Postgraduate Education Innovation Project in Shanxi Province of China, grant number 2022Y671.

**Data Availability Statement:** The data presented in this study are available on request from the corresponding author. The data are not publicly available due to data being classified.

**Acknowledgments:** The authors thank to the Institute of Energy Storage Technology for providing experimental support.

**Conflicts of Interest:** The authors declare no conflict of interest.

## References

- Li, H.; Xu, X. Solid State lithium battery research and development vision and strategy. *Energy Storage Sci. Technol.* **2016**, *5*, 607–614.
- Huang, H.; Huang, Q. Mechanism of recycling electrode materials spent lithium batteries by ball milling-low temperature heat treatment-flotation. *Chin. J. Nonferrous Met.* **2019**, *29*, 878–886.
- Jia, L.; Song, H.; Wang, H.; Fei, F.; Liu, X. Research progress of capacity optimization for second-use of electric vehicle batteries in energy storage system. *Sci. Technol. Eng.* **2018**, *18*, 153–159.
- Liu, X.; Wang, H.; Sun, Q.; Yang, J. Research progress of graphene and 3D graphene composites. *Chem. Ind. Eng. Prog.* **2018**, *1*, 168–174.
- Vetter, J.; Novák, P.; Wagner, M.R.; Veit, C.; Möller, K.C.; Besenhard, J.O.; Winter, M.; Wohlfahrt-Mehrens, M.; Vogler, C.; Hammouche, A. Ageing mechanisms in lithium-ion batteries. *J. Power Sources* **2005**, *147*, 269–281. [[CrossRef](#)]
- Hawley, W.B.; Li, J.L. Electrode manufacturing for lithium-ion batteries-Analysis of current and next generation processing. *J. Energy Storage* **2019**, *25*, 16. [[CrossRef](#)]
- Jaiser, S.; Muller, M.; Baunach, M.; Bauer, W.; Scharfer, P.; Schabel, W. Investigation of film solidification and binder migration during drying of Li-Ion battery anodes. *J. Power Sources* **2016**, *318*, 210–219. [[CrossRef](#)]
- Chu, Z.; Wang, Y. *In Theory and Engineering Practice of Infrared Radiation Heating Drying*; Chemical Industry Press: Beijing, China, 2019.
- Tan, M.; Liu, W.D.; Shi, X.L.; Sun, Q.; Chen, Z.G. Minimization of the electrical contact resistance in thin-film thermoelectric device. *Appl. Phys. Rev.* **2023**, *10*, 9. [[CrossRef](#)]
- Rossi, S.; Neues, L.; Kicokbusch, T. Thermodynamics and energetic evaluation of a heat pump applied to drying of vegetables. *Drying* **1992**, *92*, 1475–1478.
- Zhang, H. *Chemical Industry Process and Equipment*; Higher Education Press: Beijing, China, 1957.
- Ginzberg, A.C. *Principles and Technical Foundations of Food Drying*; Light Industry Press: Beijing, China, 1986.
- Chen, M.; Pan, H.; Qi, M. *Principles of Chemical Engineering, Shanghai*; East China University of Science and Technology Press: Hefei, China, 2019.
- Liu, G. Study on Unsteady Physical Parameters and Drying Characteristics of Porous Materials. Ph.D. Thesis, Kunming University of Science and Technology, Kunming, China, 2015.
- Pan, Y.K.; Wu, H.; Li, Z.Y. Effect of a tempering period on drying of carrot in a vffiro-fluidized bed. *Dry. Technol.* **1997**, *15*, 2037–2043. [[CrossRef](#)]

16. Zhu, Z.Q.; He, Y.L.; Hu, H.J.; Zhang, F.Z. Evolution of Internal Stress in Heterogeneous Electrode Composite during the Drying Process. *Energies* **2021**, *14*, 15. [[CrossRef](#)]
17. Yang, J.H.; Li, X.; Chu, Z.; Jiao, S.; Li, C.; Jiang, J. Optimization of heat and mass transfer mechanism of grain by infrared radiation vibration fluidization. *J. Eng. Thermophys.* **1996**, *4*, 452–456.
18. Jaiser, S.; Friske, A.; Baunach, M.; Scharfer, P.; Schabel, W. Development of a three-stage drying profile based on characteristic drying stages for lithium-ion battery anodes. *Dry. Technol.* **2017**, *35*, 1266–1275. [[CrossRef](#)]
19. Shi, T.; Chen, Y. *Computational Heat Transfer*; Science and Technology Press: Beijing, China, 1987.
20. Susarla, N.; Ahmed, S.; Dees, D.W. Modeling and analysis of solvent removal during Li-ion battery electrode drying. *J. Power Sources* **2018**, *378*, 660–670. [[CrossRef](#)]
21. Datta, A.K. Porous media approaches to studying simultaneous heat and mass transfer in food processes. I: Problem formulations. *J. Food Eng.* **2007**, *80*, 80–95. [[CrossRef](#)]
22. Purlis, E. Modelling convective drying of foods: A multiphase porous media model considering heat of sorption. *J. Food Eng.* **2019**, *263*, 132–146. [[CrossRef](#)]
23. Joardder, M.U.H.; Kumar, C.; Karim, M.A. Multiphase transfer model for intermittent microwave-convective drying of food: Considering shrinkage and pore evolution. *Int. J. Multiph. Flow* **2017**, *95*, 101–119. [[CrossRef](#)]
24. Lu, T. Research and Application of Heat and Mass Transfer Model in Drying Process of Capillary Porous Medium. Ph.D. Thesis, Dalian University of Technology, Dalian, China, 2003.
25. Turner, I.W.; Ilic, M. Convective drying of a consolidated slab of wet porous material. *Int. J. Heat Mass Transf.* **1990**, *17*, 39–48. [[CrossRef](#)]
26. Lu, T.; Shen, S.Q. Numerical and experimental investigation of paper drying: Heat and mass transfer with phase change in porous media. *Appl. Therm. Eng.* **2007**, *27*, 1248–1258. [[CrossRef](#)]
27. Doster, F.; Hilfer, R. Corrigendum: Generalized Buckley–Leverett theory for two-phase flow in porous media. *New J. Phys.* **2012**, *14*, 2090–2096. [[CrossRef](#)]
28. Demond, A.H.; Roberts, P.V. Effect of interfacial forces on two-phase capillary pressure-saturation relationships. *Water Resour. Res.* **1991**, *27*, 423–437. [[CrossRef](#)]
29. Halder, A.; Datta, A.K. Surface heat and mass transfer coefficients for multiphase porous media transport models with rapid evaporation. *Food Bioprod. Process.* **2012**, *90*, 475–490. [[CrossRef](#)]
30. Kumar, C.; Joardder, M.U.H.; Farrell, T.W.; Millar, G.J.; Karim, A. A porous media transport model for apple drying. *Biosyst. Eng.* **2018**, *176*, 12–25. [[CrossRef](#)]
31. COMSOL. *Evaporation in Porous Media with Large Evaporation Rates*; COMSOL Multiphysics 5.4; COMSOL: Stockholm, Sweden, 2018.

**Disclaimer/Publisher’s Note:** The statements, opinions and data contained in all publications are solely those of the individual author(s) and contributor(s) and not of MDPI and/or the editor(s). MDPI and/or the editor(s) disclaim responsibility for any injury to people or property resulting from any ideas, methods, instructions or products referred to in the content.